

PAPER

Hyaluronic acid modified Cu/Mn-doped metalorganic framework nanocatalyst for chemodynamic therapy

To cite this article: Xiaohuan Guo et al 2024 Biomed. Mater. 19 065025

View the article online for updates and enhancements.

You may also like

- CeO₂@CuS@PDA-FA as targeted nearinfrared PTT/CDT therapeutic agents for cancer cells

Jing Zhang, Miaomiao Hu, Changchun Wen et al.

- A Swing of the Pendulum: The Chemodynamics of the Local Stellar Halo Indicate Contributions from Several Radial Merger Events

Thomas Donlon and Heidi Jo Newberg

 - 3D-printed bioceramic scaffolds with Fe₃S₄ microflowers for magnetothermal and chemodynamic therapy of bone tumor and regeneration of bone defects
Hui Zhuang, Chen Qin, Meng Zhang et al.



Biomedical Materials



8 July 2024

REVISED

29 August 2024

ACCEPTED FOR PUBLICATION 1 October 2024

PUBLISHED 10 October 2024

PAPER

Hyaluronic acid modified Cu/Mn-doped metal-organic framework nanocatalyst for chemodynamic therapy

Xiaohuan Guo, Qi Fang, Nan Leng, Yuan Liu, Bingbing Cai, Yuzhu Zhou and Changchun Wen* 📵



State Key Laboratory for Chemistry and Molecular Engineering of Medicinal Resources, Key Laboratory for Chemistry and Molecular Engineering of Medicinal Resources (Ministry of Education of China), Collaborative Innovation Center for Guangxi Ethnic Medicine, School of Chemistry and Pharmaceutical Sciences, Guangxi Normal University, Guilin 541004, People's Republic of China Author to whom any correspondence should be addressed.

E-mail: wcchun@163.com

Keywords: chemodynamic therapy, tumor targeting, metal-organic framework, nanocatalyst Supplementary material for this article is available online

Abstract

Chemodynamic therapy (CDT) is a new method for cancer treatment that produces highly toxic reactive oxygen species (ROS) in the tumor microenvironment to induce cancer cell apoptosis or necrosis. However, the therapeutic effect of CDT is often hindered by intracellular H₂O₂ deficiency and the activity of antioxidants such as glutathione (GSH). In this study, a nano-catalyst HCM was developed using a self-assembled Cu/Mn-doped metal-organic framework, and its surface was modified with hyaluronic acid to construct a tumor-targeting CDT therapeutic agent with improved the efficiency and specificity. Three substances HHTP (2, 3, 6, 7, 10, 11-hexahydroxybenzophenanthrene), Cu²⁺, and Mn²⁺ were shown to be decomposed and released under weakly acidic conditions in tumor cells. HHTP produces exogenous H₂O₂ in the presence of oxygen to increase the H₂O₂ content in tumors, Cu²⁺ reduces GSH content and generates Cu⁺ in the tumor, and Cu⁺ and Mn²⁺ catalyze H₂O₂ to produce ·OH in a Fenton-like reaction. Together, these three factors change the tumor microenvironment and improve the efficiency of ROS production. HCM showed selective and efficient cytotoxicity to cancer cells, and could effectively inhibit tumor growth in vivo, indicating a good CDT effect.

1. Introduction

Cancer poses a serious threat to human life and health. Although traditional cancer treatment methods such as surgical resection, chemotherapy and radiotherapy have positive therapeutic effects, there remain still face great challenges including overcoming multi-drug resistance and tumor pathological complexity, as well as preventing recurrence and metastasis. In addition, toxic side-effects of chemotherapy, damage to healthy tissue by radiotherapy, and the invasive nature of surgery are all key issues that need to be addressed [1, 2]. In recent years, various novel cancer treatment strategies have emerged, including immunotherapy, photothermal therapy, photodynamic therapy, sonodynamic therapy, and chemodynamic therapy (CDT). However, immunotherapy is not universal, and photothermal therapy, photodynamic therapy, and sonodynamic therapy

rely on external energy sources such as light or sound waves to trigger therapeutic effects [3-6]. By contrast, CDT uses the tumor microenvironment to generate reactive oxygen species (ROS) through Fenton or Fenton-like reactions. Therefore, this approach is more flexible and controllable and especially conducive to the treatment of deep tumors, its advantages also include precise targeting, reduced side-effects, and the ability to overcome multi-drug resistance [7–11]. CDT is triggered by the endogenous tumor microenvironment. In the presence of metal ions such as Fe²⁺, Cu⁺, Mn²⁺, Co²⁺, or Mo⁵⁺, Fenton or Fenton-like reactions convert endogenous H₂O₂ into highly active hydroxyl radicals (·OH) which are more toxic to tumor cells than other ROS with respect to the induction of apoptosis [12–15]. The severe toxicity of ·OH causes irreversible damage to biological molecules (such as DNA, lipids, and proteins), which can kill tumor cells [16–19].

CDT is a treatment mode that combines Fenton chemistry with characteristics of the tumor microenvironment which include low pH, high H₂O₂ concentration, hypoxia, low catalase activity, and high concentrations of glutathione (GSH), hydrogen sulfide, and phosphate [20]. The higher H_2O_2 concentration and lower pH of the tumor microenvironment compared with normal tissue is beneficial for Fenton/Fenton-like reactions [21-23] and means that more ·OH can be produced in tumor tissues [24]. However, some CDT drugs show poor therapeutic effects, usually owing to insufficient endogenous H₂O₂. In addition, the high concentration of GSH in the tumor microenvironment often consumes the generated ·OH to maintain redox homeostasis, greatly reducing the efficiency of CDT [18, 25].

Chemotherapeutic agents can be used to generate endogenous H2O2 with significant potential to improve the effects of CDT. HHTP (2,3,6,7,10,11hexahydroxytriphenyl) is an organic polyphenol ligand that can generate O2- and H2O2 via singleelectron and double-electron oxidation [26-31]. In addition, the rapid electron transfer characteristics of the catechol/quinone group in HHTP can accelerate electron transfer between metals [22, 32]. Nanocatalysts constructed of by combining catechol with metals can be used to disrupt the redox homeostasis of drug-resistant cells, thereby enhancing cellular oxidative capacity, this approach can achieve selectivity and high cytotoxicity against a variety of drug-resistant cancer cells. In addition, active metal ions (such as Fe3+, Cu2+, and Mn4+) can effectively oxidize GSH to GSH disulfide, thereby reducing GSH content. Low-valent metal ions (such as Fe²⁺, Cu⁺, and Mn²⁺) can also be used for CDT [10, 33]. Metal-organic frameworks are a unique type of inorganic-organic hybrid crystalline materials that self-assembles from metal ions and organic linkers. They exhibit adjustable structures, high porosity, ease of modification, strong stimulus responsiveness, and excellent biocompatibility/biodegradability [34-37]. In particular, metal-organic frameworks that are degraded in the tumor microenvironment can be constructed with metal ions that consume GSH and have Fenton or Fenton-like reactivity as nodes, making them ideal candidates as CDT agents [15, 38, 39]. Hyaluronic acid (HA), a linear polysaccharide with good biocompatibility and low immunogenicity, is an important component of the extracellular matrix. CD44, the main HA receptor, is often overexpressed in tumor cells and binds to HA with a high affinity. HA can target tumors through the CD44 receptor endocytosis pathway [40–43].

Herein, we synthesized a bimetallic metal-organic framework nanocatalyst with catechol as the organic ligand and Cu and Mn as coordination atoms and modified its surface with HA to construct tumortargeting CDT agents. The agents were endocytosed into tumor cells by binding of HA on the surface

to CD44 receptors specific to tumor cells. In the weakly acidic tumor microenvironment, the metalorganic framework breaks down, and Cu^{2+} , Mn^{2+} , and HHTP are released. Cu^{2+} reacts with the abundant GSH in tumor cells through a redox reaction, which generates Cu^+ . The Cu^+ and Mn^{2+} catalyzes H_2O_2 to produce toxic ·OH through a Fenton-like reaction. Moreover, HHTP and intracellular oxygen generate H_2O_2 and promote Fenton-like reactions of Cu^+ and Mn^{2+} , there by producing larger amounts of ·OH and improving the efficacy of the CDT (scheme 1).

2. Material and methods

2.1. Materials

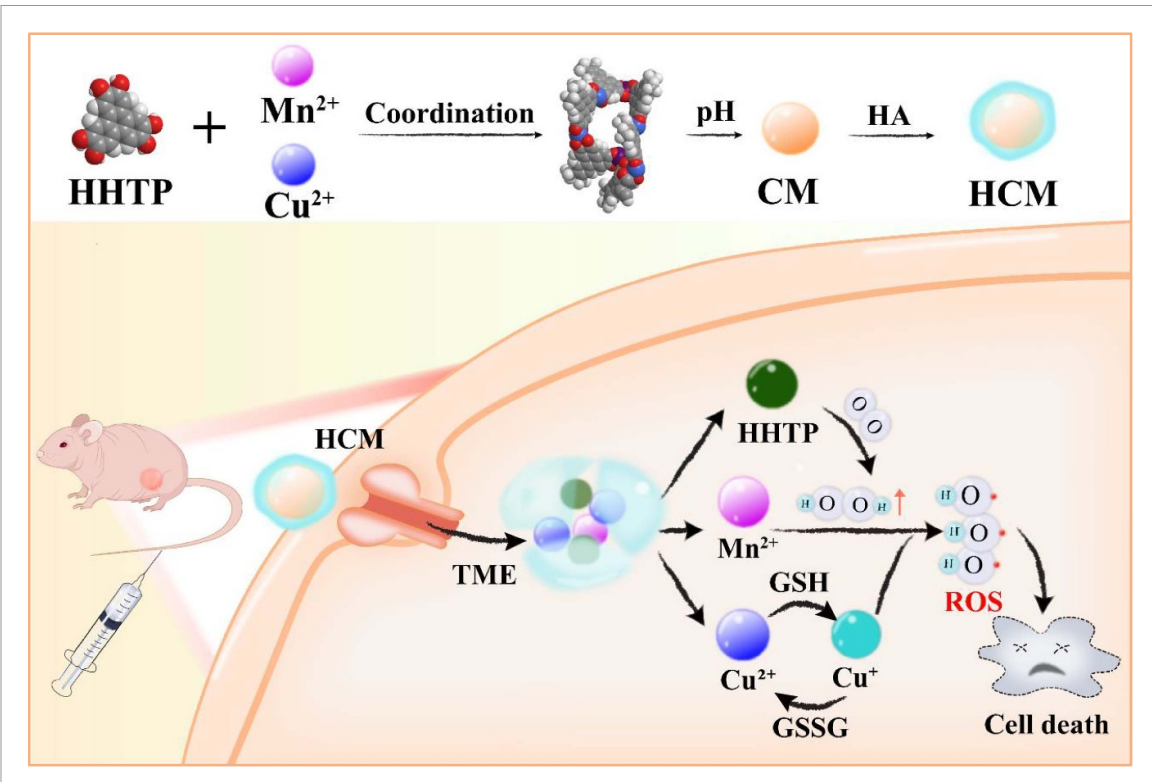
2,3,6,7,10,11-hexahydroxytriphenylene, Cu(Ac)₂·H₂O, and Mn(Ac)2 were purchased from the Aladdin Reagent Company (Shanghai, China). 2',7'-Dichlorodihydrofluorescein diacetate (DCFH-DA), calcein acetoxymethyl ester (Calcein-AM) and propidium iodide (PI) dyes were purchased from Beyotime Biotechnology (Shanghai, China). 3-(4,5dimethylthiazole-2-yl)-2,5-diphenyl tetrazoliume bromide (MTT) and Tris-HCl were purchased from Beijing Solaibao Technology Company (Beijing, China). Other liquid chemical reagents were purchased from Xilong Science Company (Sichuan, China). Both tumor cell lines and normal cell lines were derived from the cell bank of the Chinese Academy of Sciences. The mice were SPF BALB/c nude mice, aged 5-6 weeks, 15-18 g, female, purchased from Hangzhou Ziyuan Laboratory Animal Technology Co., Ltd

2.2. Synthesis of Cu/Mn doped nanocatalyst

Cu(Ac)₂·H₂O (5.5 mg) and Mn(Ac)₂ (5.5 mg) were dissolved in 5 ml water, and HHTP (32.4 mg) was dissolved in 10 ml DMSO. Subsequently a Cu/Mndoped metal solution was added to HHTP solution and stirred at 25 °C for 10 min. Subsequently, the mixture was adjusted with 1.5 M Tri-HCl buffer pH 8.8 to pH 7.5, and stirring was continued for 1 h. The precipitate was washed three times with methanol and water and then dried.

2.3. Synthesis of HCM

HCM was synthesized according to the method described by Hao *et al* [44, 45]. In brief, the Cu/Mn doped nanocatalyst (CM) (4 mg) and HA (8 mg) were dissolved separately in 2 ml deionized water. Then, the CM solution was added to the HA solution and the mixture solution was ultrasonicated at room temperature for 30 min. Then, the reaction was carried out at 25 °C for 48 h. Then, the mixture was centrifuged at 10 000 rpm for 10 min, the supernatant was removed, and the precipitate was washed twice with deionized water and freeze-dried to obtain HCM.



Scheme 1. Schematic illustration of the synthesis of the hyaluronic acid-modified Cu/Mn doped metal-organic framework nanocatalyst for CDT. (HHTP: 2,3,6,7,10,11-hexahydroxytriphenylene, CM: Cu/Mn doped metal-organic framework, HA: hyaluronic acid, TME: tumor microenvironment).

2.4. Characterization

The morphologies of CM and HCM were characterized using transmission electron microscopy (TEM) (Talos F200 G2) and scanning electron microscopy (SEM) (Quanta 200 FEG). The zeta potential and particle size were measured using a Malvern Zetasizer Nano ZS instrument, the UV-vis absorption spectra were determined using a Shimadzu UV-2600 spectrophotometer, and a Spectrum Two FT-IR spectrometer was used to determine the functional groups of the materials. The chemical compositions and structures of the samples were studied using a Rigaku DMAX-2500 x-ray diffractometer and a Nexsa x-ray photoelectron spectrometer. Cell viability was measured using BioTek Cytation5, and cell morphology and staining were observed using the EVOSFLAuto2 automatic cell imaging system.

2.5. ROS detection

In a solution containing 10 μ g ml⁻¹ Methylene blue (MB), one or more of various reagents (100 μ M H₂O₂, 50 μ g ml⁻¹ CM, and 3 mM GSH) was added and left standing for 60 min in 37 °C water bath. The ·OH induced MB degradation was monitored based on the changes in absorbance at 665 nm to evaluate the formation of ·OH via the Cu⁺/Mn²⁺-mediated Fenton-like reaction and the scavenging of ·OH by GSH. The effects of different concentrations of GSH (0, 0.5, 1, 2, and 3 mM), different concentrations of CM (0, 25, 50, 75, 100 μ g ml⁻¹) or different pH (5.0,

6.5, and 7.4) on MB degradation were also investigated when other conditions were unchanged.

2.6. Cytotoxicity in vitro

A standard MTT assay was used to estimate the cytotoxicity of HCM *in vitro* and the combined efficacy of CDT. 4T1 cells in suspension were inoculated into a 96-well plate and cultured in a sterile incubator at 37 °C for 12 h, the Cell density reached 60%–70% of each well, CM solution and HCM solution were added (0, 3.12, 6.25, 12.5, 50 and 100 μ g ml⁻¹) and incubation continued for 24 h. After incubation for 24 h, 5 mg ml⁻¹ MTT solution was added, and the incubation was continued for another 4–6 h. Then, the liquid was removed from the wells, DMSO solution was added, and the plate was placed on a shaking table for 10 min to fully dissolve enable the purple crystals. The absorbance of each well (n=4) at 570 nm was measured using a Cytation5 instrument.

2.7. Cell uptake

Cells were inoculated in a 7 cm petri dish. After the cells had grown to 70%–80% of the total volume, 100 µg ml⁻¹ HCM was added, followed by culture for 24 h, a no-drug group was used as a blank control. After incubation, the cells were digested with trypsin, and the collected cell suspension was transferred to a centrifuge tube and centrifuged at 1200 rpm for 10 min, then the supernatant was removed, and 5 ml phosphate-buffered saline (PBS) was added for washing, followed by centrifugation for a further 5 min.

After removal of as much PBS as possible, 1 ml nitric acid and 500 μ l 30% hydrogen peroxide were added, and nitration was performed at room temperature for 24 h. Finally, 100 μ l of the solution was taken, diluted to 2 ml with ultra-pure water, and mixed well. Inductively coupled plasma mass spectrometry (ICP-MS) was used to detect the copper and manganese content.

2.8. ROS detection in vitro

The cell suspension was inoculated into a six-well plate and cultured in a sterile incubator. When the cell density reached 60%, RPMI 1640 medium (containing 10% (v/v) fetal bovine serum) and 100 µg ml⁻¹ CM or HCM were added, and the cells were incubated for 4 h or 8 h, respectively. The ROS probe DCFH-DA was diluted with PBS at a ratio of 1:1000 and co-incubated with the cells 30 min at 37 °C in the dark. Finally, the intracellular fluorescence intensity was observed using an EVOSFLAuto2 automatic cell imaging system to determine ROS levels.

2.9. Live and dead cell staining

The cell suspension was inoculated into a six-well plate and cultured in a sterile incubator. When the cell density reached 70%, RPMI 1640 medium and 100 μg ml⁻¹ CM or HCM were added. After incubation for 8 h, calcein-AM and PI (live and dead cell probes) were diluted with PBS at a ratio of 1:1:2000 and co-incubated with the cells for 30 min at 37 °C in the dark. Finally, intracellular fluorescence intensity was observed using an EVOSFL Auto 2 to determine levels of live and dead cells. The degree of staining was analyzed statistically using ImageJ.

2.10. *In vivo* CDT therapy

A 4T1 tumor-bearing mouse model was used to study the therapeutic effects of HCM *in vivo*. Briefly, when tumor volumes reached approximately 60–100 mm³, the mice were randomly divided into two groups (n=3) and treated with saline or HCM. The drug was administered intravenously daily (100 μ l, 100 μ g ml⁻¹), and mouse weights and tumor volumes were measured every 2 d. The formula used to calculate tumor volume was $V=W^2L/2$ (where V is the volume, and W and L are the width and length of the tumor, respectively). The animal experiment plan has passed the ethics review of the Experimental Animal Ethics Committee of Guangxi Normal University, and the ethics review acceptance number is GXNU-202 403-043.

3. Discussion and results

3.1. Synthesis and characterization

HCM was prepared via coordination and self-assembly. First, Cu(Ac)₂·H₂O and Mn(Ac)₂ were dissolved in water, and HHTP was dissolved in dimethyl

sulfoxide. The HHTP solution was mixed with the metal solution and stirred, then Tri-HCl buffer solution was added, with continued stirring to form CM. Next, the CM and HA were dissolved in deionized water. After ultrasound treatment, the reaction was stirred again, and HCM was obtained. HHTP contains six hydroxyl groups with good coordination abilities with copper and manganese. Therefore, the two metals and hydroxyl groups could be connected through metal coordination bonds, and then selfassembled to form a metal organic framework material by adjusting the pH. Finally, HA was wrapped on the surface of the CM through electrostatic adsorption to synthesize HCM (scheme 1). The morphology and elements of the nanocatalyst were characterized using SEM (figure 1(a)) and TEM (figure 1(b)). The CM was observed to be irregularly spherical with a size of approximately 250 nm, whereas HCM was similar but slightly larger, with a size of about 300 nm. The particle size obtained by electron microscopy was slightly smaller than the hydrodynamic size obtained by dynamic light scattering (figure 2(a)) with hydrodynamic sizes of CM and HCM of 295 and 342 nm, respectively. This was because the hydrodynamic size obtained by dynamic light scattering is related to the core of the nanoparticle and the expanded corona, resulting in a larger particle size, whereas TEM usually obtained the core size in the dry state, with low electron density and invisibility. High-angle annular dark-field scanning TEM (HAADF-STEM) images and element mapping spectrum images of the HCM were obtained (figure 1(c)), which showed that HCM consisted of C, O, N, Cu, and Mn. The HCM contained N owing to modification with HA.

The zeta potentials of CM and HCM (figure 2(b)) were -0.58 ± 0.09 and -28.70 ± 0.72 , respectively, indicating effective modification with HA. In the ultraviolet-visible absorption spectrum (figure 2(c)), the absorption peak showed a redshift owing to conjugation between HHTP and the metal coordination after self-assembly. In the Fourier transform infrared spectra of HHTP and CM (figure 2(d)), the absorption peak corresponding to the C-O-H bond in HHTP at 1058 cm⁻¹ was absent from CM spectrum. Importantly, there was a characteristic peak at 568 cm⁻¹, corresponding to the Cu–O bond, providing a preliminary indication that Cu and O coordination has been successful. After coating with HA, HCM exhibited a new absorption peak at 3692 cm⁻¹, which was attributed to the stretching vibration of the free hydroxyl group on HA. X-ray photoelectron spectra and x-ray diffractometry spectra were used to analyze the chemical composition and structure of CM and HCM. In the x-ray diffractometry spectra pattern of CM (figure 2(e)), diffraction peaks were observed at 4.76°, 9.56°, 12.60°, 16.68°, and 27.64°, each of these matched well with those reported for CuHPT in the literature [26], indicating that the framework had

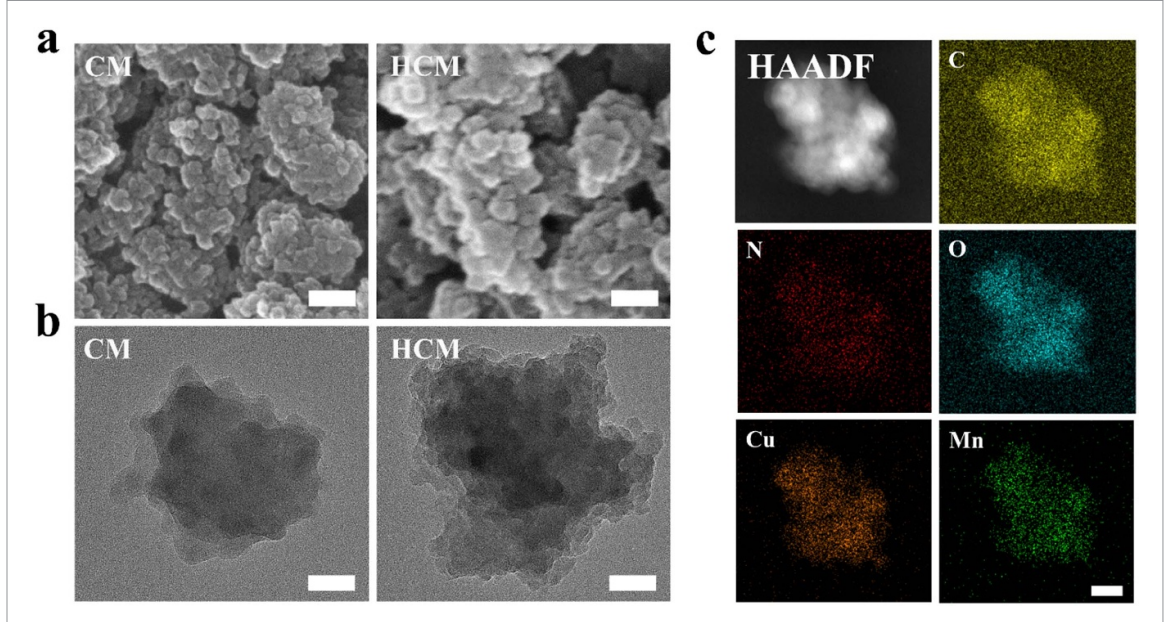


Figure 1. (a) SEM images of CM and HCM (scale bar: 100 nm). (b) TEM images of CM and HCM (scale bar: 50 nm). (c) HAADF-STEM image of HCM, corresponding element mapping spectrum of C, N, O, Cu, Mn. (scale bar: 50 nm).

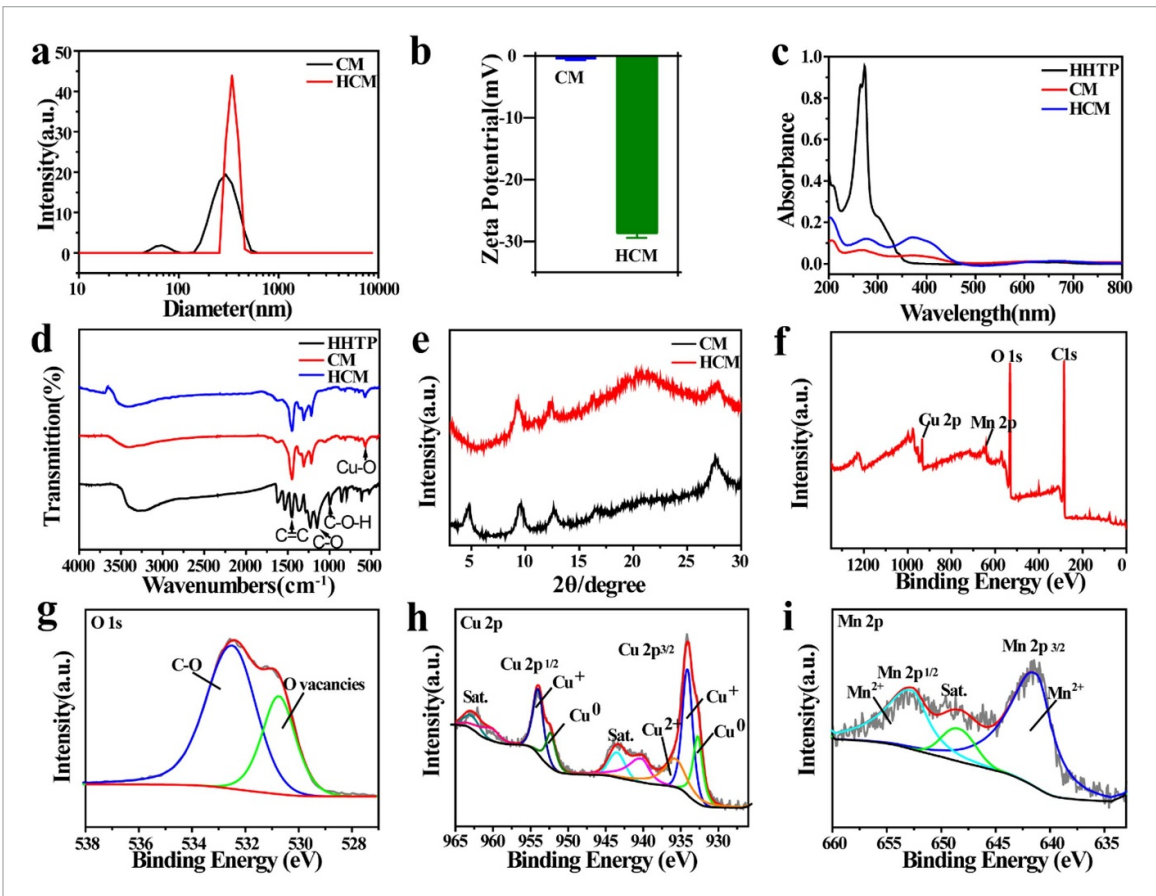


Figure 2. (a) Dynamic light scattering data of CM and HCM. (b) Zeta potentials of CM and HCM. (c) Ultraviolet–visible absorption spectra of HHTP, CM and HCM. (d) Fourier transform infrared spectra of HHTP, CM and HCM. (e) X-ray diffractometry spectra pattern of CM and HCM. (f)–(i) XPS of CM.

been successfully synthesized. As CM retained the original crystal structure of CuHPT according to the x-ray diffractometry spectra, the influence of Mn doping on the crystal structure was negligible [8]. In addition, the main diffraction peaks of CM did not change

after HA coating, indicating that HA coating had little effect on the crystal structure of CM.

The nanocatalyst was further studied using XPS. The full XPS (figure 2(f)) showed that CM is composed of C, O, Cu, and Mn. The fitting spectrum of

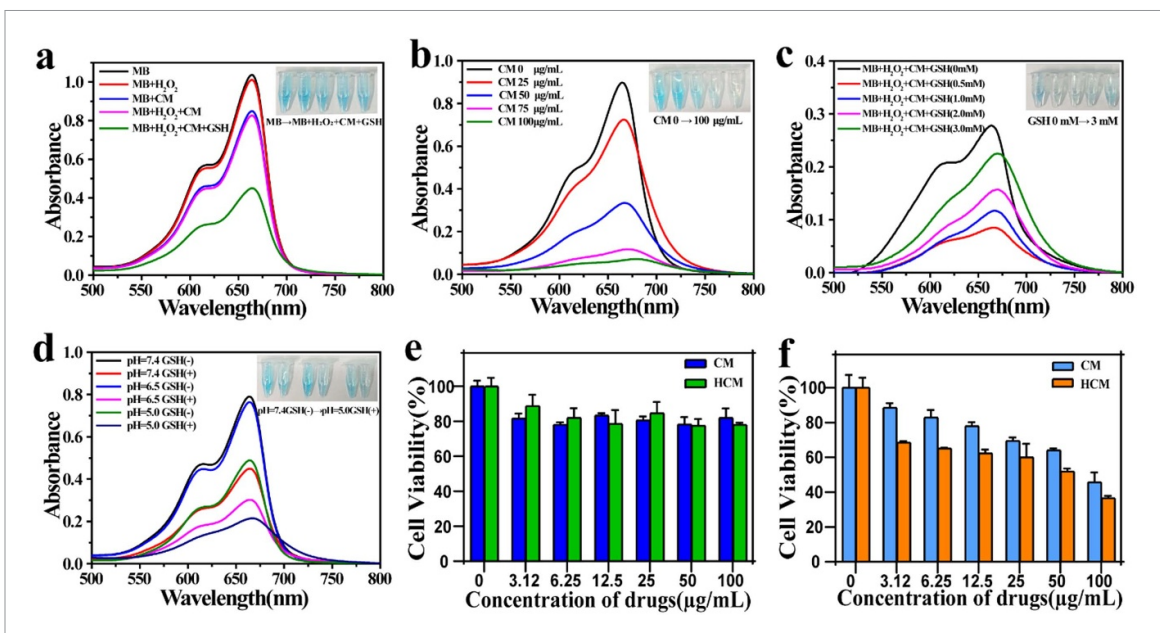


Figure 3. Degradation ability of methylene blue under different conditions. (a) Addition of different substrate. (b) Varying CM concentrations. (c) Varying GSH concentrations. (d) Varying pH in the presence or absence of GSH. Relative viabilities of L-929 cells (e) and 4T1 cells (f) after being incubated with CM or HCM at different concentrations for 24 h.

XPS (table S1), the atomic percentage of Cu and Mn were 2.07 and 1.00. As calculated by ICP-MS, the proportion of Cu in CM was approximately 15%, whereas that of Mn was 7%, consistent with the metal proportions obtained by XPS. The peaks at binding energies 530.78 eV and 532.58 eV in the O 1s spectrum (figure 2(g)) were attributed to C–O and O vacancies, respectively. The 530.79 eV was derived from ligands, 532.58 eV indicated that O could be coordinated with metals. In the Cu 2p (figure 2(h)), the peaks at binding energies of 932.78 eV, 934.18 eV, and 935.88 eV belonged to Cu⁰, Cu⁺ and Cu²⁺, respectively. The presence of Cu⁺ and Cu⁰ indicated that some Cu²⁺ was reduced during the synthesis of the material. Similarly, in the Mn 2p spectrum (figure 2(i)), the peak with a binding energy of 641.68 eV could be attributed to Mn²⁺. The XPS of HCM was not significantly different from that of CM (figure S1). The presence of low-valent metals and electron transfer between the metals are expected to improve the efficiency of Fenton-like reactions.

3.2. Chemodynamic properties of HCM

The characterization presented above suggested that the catalyst would have a positive effect on the efficacy of CDT. The CDT properties of HCM are completely dependent on CM, therefore, the CDT properties of HCM could be verified by examining the ROS generation capacity of CM. This was investigated using MB and *in vitro* cell experiments. MB degradation mediated by \cdot OH can be used to detect the formation of \cdot OH. Therefore, the effects of various substrates on MB degradation were examined (figure 3(a)). Addition of H₂O₂ to the MB solution

slightly weakened the absorption peak at 665 nm and enhanced MB degradation to a small extent. However, when only CM was added to the MB solution, MB degradation was further enhanced because of the oxidation of HHTP to form ROS (O₂⁻ and H₂O₂). Moreover, the rapid electron transfer characteristics of the catechol/quinone groups in HHTP accelerated the electron transfer between metals, leading to degradation of MB by the resulting ·OH. Finally, the newly added GSH reacted with Cu²⁺ to produce Cu⁺, whereas Cu⁺ and Mn²⁺ reacted with H₂O₂ to produce more ·OH, resulting in the strongest MB degradation effect. Next, the effects of different CM concentrations on the degradation of MB in the presence of GSH and H₂O₂ were examined (figure 3(b)). As the CM concentration increased, the intensity of the absorption peak at 665 nm gradually decreased, indicating that MB degradation gradually increased. Treatment with HCM had a similar effect to CM at the same concentration (figure S2). Subsequently the effects of different GSH concentrations on MB degradation in the presence of H₂O₂ and CM were investigated (figure 3(c)). In the concentration range of 0-0.5 mM, the absorption peak intensity gradually decreased with increasing GSH concentration, owing to the reaction of Cu²⁺ with GSH to form Cu⁺ and GSSG, followed by the reaction of Cu⁺ and Mn²⁺ with H₂O₂ to form ·OH, which resulted in MB degradation. When the concentration of GSH was greater than 0.5 mM, the absorption peak at 665 nm was enhanced, because excess GSH could remove ·OH. Finally, the effects on MB degradation at different pH values, with or without GSH, in the presence of H_2O_2 and CM, were investigated (figure 3(d)).

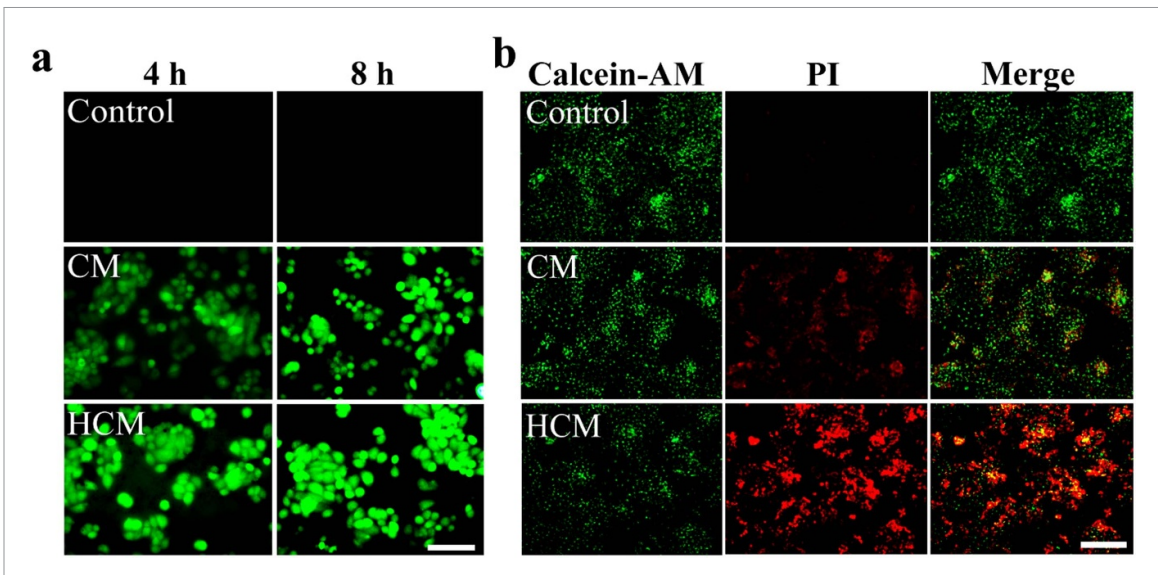


Figure 4. (a) ROS generation (green fluorescence) of 4T1 cells at 4 h and 8 h after different treatments (scale bar: 100 μm). (b) Staining of live and dead 4T1 cells (green and red fluorescence, respectively) after different treatments for 8 h (scale bar: 200 μm).

At pH 5.0 and in the presence of GSH, CM showed strong MB degradation ability and could produce more ·OH.

3.3. CDT antitumor effects in vitro

Given that CM had shown good ·OH-generating ability, its antitumor effects on 4T1 cells were further studied using the MTT method. After treatment with 100 μg ml $^{-1}$ CM and HCM, L-929 cells maintained a high survival rate, indicating that the nanocatalysts had good stability under neutral conditions and did not decompose prematurely (figure 3(e)). By contrast, HCM showed strong cytotoxicity against 4T1 cells, with a survival rate of 36% at 100 μg ml $^{-1}$ (figure 3(f)). According to calculations performed in GraphPad, the half-maximal inhibitory concentrations of CM and HCM for 4T1 cells were 93.87 μg ml $^{-1}$ and 43.55 μg ml $^{-1}$, respectively. Thus, HCM is less toxic to normal cells in comparison with tumor cells.

To explore the targeting properties of the material, ICP-MS was used to detect the total uptake of HCM by L-929 and 4T1 cells (figure S3). After incubation of the cells with HCM for 24 h, the Cu and Mn contents of the cells in the drug-treated group were increased compared with those in the control group. The copper contents of HCM in L-929 and 4T1 cells was 12.41 \pm 0.11 and 69.17 \pm 0.56 $\mu g \, l^{-1}$, whereas the manganese contents were 1.49 \pm 0.03 and 6.45 \pm 0.04 $\mu g \, l^{-1}$, respectively, after subtracting the respective contents of the cells in the control group. That is, the uptake of of HCM was greater in cancer cells than in normal cells, demonstrating the targeting ability of the material.

Subsequently, to evaluate the effects of HCM on ROS generation, DCFH-DA was used to detect changes in intracellular ROS levels (figures 4(a) and S4(a)). After incubation with RPMI 1640 medium

(containing 10% (v/v) fetal bovine serum), CM, and HCM for 4 and 8 h, 4T1 cells showed significantly increased ROS levels. As the MTT cytotoxicity experiment had confirmed that CM and HCM were toxic to 4T1 cells, fluorescence microscopy was used to further study this toxicity by detecting live and dead cells stained with calcein-AM and PI, respectively (figures 4(b) and S4(b)). After incubation of cells with RPMI 1640 medium, CM, and HCM, the proportion of live cells (green fluorescence) significantly decreased, whereas that of dead cells (red fluorescence) significantly increased, demonstrating the good anticancer activity of HCM.

3.4. CDT antitumor effects in vivo

The results of the *in vitro* experiments prompted us to further investigate the potential antitumor effects of HCM in vivo, using a 4T1 tumor-bearing mouse model was used to evaluate the therapeutic effect of HCM. When the tumor volumes reached 60-100 mm³, the mice were divided into two groups: a control group (treated with saline) and a treatment group (treated with HCM). The drug was administered intravenously, and the body weights and tumor volumes of the mice were monitored daily during the 14 d treatment period. Any changes in body weight within this period were insignificant and negligible in both groups (figure 5(a)). As shown in figure 5(b), the tumor growth rate was slower in the HCM treatment group compared with the normal saline group. The changes in tumor weight in the two groups showed that HCM had an antitumor effect (figure 5(c)). As shown in figure 5(d), after 14 d of CDT with HCM, the tumors in the treatment group were significantly smaller than those in the saline control group. Photographs of the tumor tissues after 14 d of treatment also showed consistent results

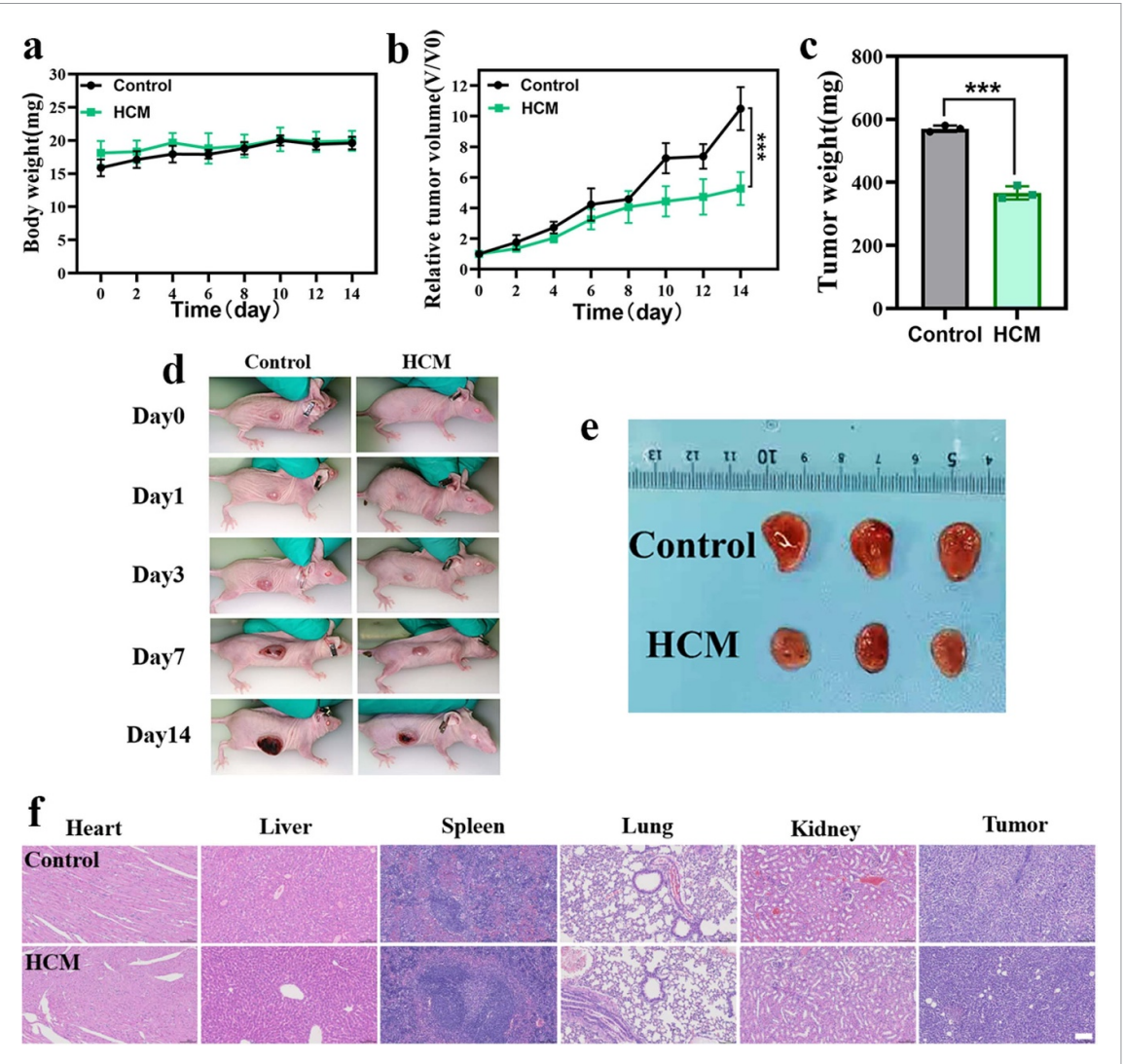


Figure 5. (a) Time-dependent body weight curves of 4T1 tumor-bearing nude mice during different administrations. (b) Time-dependent tumor growth curves. Data are expressed as the mean standard deviation (n=3). (c) Tumor weights (d) Representative photographs of the mice in different treatment groups at different treatment time points. (e) Photographs of dissecting tumor sizes after treatments. (f) The H&E staining of tumor and organs tissue with different treatments. (scale bar: $100 \mu m$).

(figure 5(e)), in agreement with the MTT assay results. Moreover, hematoxylin and eosin (H&E) staining analysis of tumor sections (figure 5(f)) showed that tumor tissues in the treatment group exhibited a degree of necrosis, which could be attributed to drug action. No significant changes were observed in the main organ sections, indicating good biosafety. These results demonstrate that the HCM treatment process caused negligible damage to mice. In summary, HCM shows a good antitumor effect and biosafety.

4. Conclusion

In summary, a novel self-assembled coppermanganese-doped nanocatalyst with high CDT efficacy was successfully designed and synthesized for targeted tumor CDT. The nanocatalyst is coated with HA and can thus be specifically transported to tumor cells to avoid damage to normal tissues. After endocytosis by tumor cells, HCM acts synergistically with HHTP, Cu, and Mn to enhance the efficacy of CDT by depleting GSH and increasing H_2O_2 content. In a breast cancer tumor model, HCM inhibited tumor growth without significant systemic toxicity compared with the saline group. Therefore, this study provides both a highly efficient CDT agent for selective killing of breast cancer cells and an example of the design of CDT nanocatalysts capable of simultaneously depleting GSH and increasing H_2O_2 content.

Data availability statement

All data supporting the findings of this study are included in the article (and any supplementary files).

Conflict of interest

The authors have no competing interests to disclose.

Funding

This stydy was financially supported by the National Natural Science Foundation of China (22064018).

Conflict of interests

The authors declare they have no financial interests.

Authors' contributions

Conceptualization-X Guo, C Wen; original draft writing-X Guo, Q Fang, C Wen; illustrations-X Guo, N Leng; proofreading-Y Liu, B Cai, Y Zhou; All authors read and approved the final manuscript.

ORCID iD

Changchun Wen https://orcid.org/0000-0002-9028-0063

References

- Pei Z, Lei H and Cheng L 2023 Bioactive inorganic nanomaterials for cancer theranostics *Chem. Soc. Rev.* 52 2031–81
- [2] Ibrahim E Y and Ehrlich B E 2020 Prevention of chemotherapy-induced peripheral neuropathy: a review of recent findings Crit. Rev. Oncol. Hemat. 145 102831
- [3] Sun D, Sun X, Zhang X, Wu J, Shi X, Sun J, Luo C, He Z and Zhang S 2024 Emerging chemodynamic nanotherapeutics for cancer treatment Adv. Healthcare Mater. 13 2400809
- [4] Zhang Q, Luo Q, Liu Z, Sun M and Dong X 2023 Nano-ROS-generating approaches to cancer dynamic therapy: lessons from nanoparticles *Chem. Eng. J.* 457 141225
- [5] Cai L, Du J, Han F, Shi T, Zhang H, Lu Y, Long S, Sun W, Fan J and Peng X 2023 Piezoelectric metal-organic frameworks based sonosensitizer for enhanced nanozyme catalytic and sonodynamic therapies ACS Nano 17 7901–10
- [6] Yang B, Chen Y and Shi J 2019 Nanocatalytic medicine Adv. Mater. 31 1901778
- [7] Zhu Y, Wang Z, Zhao R, Zhou Y, Feng L, Gai S and Yang P 2022 Pt decorated Ti₃C₂Tx MXene with NIR-II light amplified nanozyme catalytic activity for efficient phototheranostics ACS Nano 16 3105–18
- [8] Jana D and Zhao Y 2022 Strategies for enhancing cancer chemodynamic therapy performance Exploration 2 20210238
- [9] Xing Y, Xiu J, Zhou M, Xu T, Zhang M, Li H, Li X, Du X, Ma T and Zhang X 2023 Copper single-atom jellyfish-like nanomotors for enhanced tumor penetration and nanocatalytic therapy ACS Nano 17 6789–99
- [10] Hao J-N, Ge K, Chen G, Dai B and Li Y 2023 Strategies to engineer various nanocarrier-based hybrid catalysts for enhanced chemodynamic cancer therapy *Chem. Soc. Rev.* 52 7707–36
- [11] Cao C, Wang X, Yang N, Song X and Dong X 2022 Recent advances of cancer chemodynamic therapy based on Fenton/Fenton-like chemistry Chem. Sci. 13 863–89
- [12] Liu X, Jin Y, Liu T, Yang S, Zhou M, Wang W and Yu H 2020 Iron-based theranostic nanoplatform for improving chemodynamic therapy of cancer ACS Biomater. Sci. Eng. 6 4834–45
- [13] Li W, Zhou X, Liu S, Zhou J, Ding H, Gai S, Li R, Zhong L, Jiang H and Yang P 2021 Biodegradable nanocatalyst with self-supplying fenton-like ions and H₂O₂ for catalytic cascade-amplified tumor therapy ACS Appl. Mater. Interfaces 13 50760–73

- [14] Jia C, Guo Y and Wu F G 2022 Chemodynamic therapy via fenton and fenton-like nanomaterials: strategies and recent advances Small 18 e2103868
- [15] Shen W Y, Jia C P, Liao L Y, Chen L-L, Hou C, Liu Y-H, Liang H and Chen Z-F 2022 Copper(II) complexes of halogenated quinoline Schiff base derivatives enabled cancer therapy through glutathione-assisted chemodynamic therapy and inhibition of autophagy flux J. Med. Chem. 65 5134–48
- [16] Di Y, Deng R and Liu Z 2023 Optimized strategies of ROS-based nanodynamic therapies for tumor theranostics Biomaterials 303 122391
- [17] Pan Y et al 2022 Biomimetic yolk-shell nanocatalysts for activatable dual-modal-image-guided triple-augmented chemodynamic therapy of cancer ACS Nano 16 19038–52
- [18] Sang Y, Cao F, Li W, Zhang L, You Y, Deng Q, Dong K, Ren J and Qu X 2020 Bioinspired construction of a nanozyme-based H₂O₂ homeostasis disruptor for intensive chemodynamic therapy J. Am. Chem. Soc. 142 5177–83
- [19] Lin L-S et al 2018 Simultaneous fenton-like ion delivery and glutathione depletion by MnO₂ -based nanoagent to enhance chemodynamic therapy Angew. Chem., Int. Ed. 57 4902-6
- [20] Tang Z, Liu Y, He M and Bu W 2019 Chemodynamic therapy: tumour microenvironment-mediated fenton and fenton-like reactions Angew. Chem., Int. Ed. 58 946–56
- [21] Liu G, Zhu J, Guo H, Sun A, Chen P, Xi L, Huang W, Song X and Dong X 2019 Mo₂C-derived polyoxometalate for NIR-II photoacoustic imaging-guided chemodynamic/photothermal synergistic therapy *Angew. Chem.*, Int. Ed. 58 18641–6
- [22] Zhang H et al 2023 Heterostructures with built-in electric fields for long-lasting chemodynamic therapy Angew. Chem., Int. Ed. 62 e202300356
- [23] Wang S, Pang Y, Hu S, Lv J, Lin Y and Li M 2023 Copper sulfide engineered covalent organic frameworks for pH-responsive chemo/photothermal/chemodynamic synergistic therapy against cancer *Chem. Eng. J.* 451 138864
- [24] Cairns R A, Harris I S and Mak T W 2011 Regulation of cancer cell metabolism Nat. Rev. Cancer 11 85–95
- [25] Liu Y et al 2018 All-in-one theranostic nanoagent with enhanced reactive oxygen species generation and modulating tumor microenvironment ability for effective tumor eradication ACS Nano 12 4886–93
- [26] Liu J et al 2022 Copper-based metal-organic framework overcomes cancer chemoresistance through systemically disrupting dynamically balanced cellular redox homeostasis J. Am. Chem. Soc. 144 4799–809
- [27] Zhao W, Chen T, Wang W, Bi S, Jiang M, Zhang K Y, Liu S, Huang W and Zhao Q 2021 Layer-by-layer 2D ultrathin conductive Cu₃(HHTP)₂ film for high-performance flexible transparent supercapacitors Adv. Mater. Interfaces 8 2100308
- [28] Jiang L, Wang H, Rao Z, Zhu J, Li G, Huang Q, Wang Z and Liu H 2022 In situ electrochemical reductive construction of metal oxide/metal-organic framework heterojunction nanoarrays for hydrogen peroxide sensing *J. Colloid Interface* Sci. 622 871–9
- [29] Nam K W, Park S S, Dos Reis R, Dravid V P, Kim H, Mirkin C A and Stoddart J F 2019 Conductive 2D metal-organic framework for high-performance cathodes in aqueous rechargeable zinc batteries Nat. Commun. 10 4948
- [30] Zhou K, Zhang C, Xiong Z, Chen H-Y, Li T, Ding G, Yang B, Liao Q, Zhou Y and Han S-T 2020 Template-directed growth of hierarchical MOF hybrid arrays for tactile sensor Adv. Funct. Mater. 30 2001296
- [31] Cao L-A, Yao M-S, Jiang H-J, Kitagawa S, Ye X-L, Li W-H and Xu G 2020 A highly oriented conductive MOF thin film-based Schottky diode for self-powered light and gas detection J. Mater. Chem. A 8 9085–90
- [32] Zhao P, Li H and Bu W 2023 A forward vision for chemodynamic therapy: issues and opportunities Angew. Chem., Int. Ed. 62 e202210415
- [33] Wang X-Q, Wang W, Peng M and Zhang X-Z 2021 Free radicals for cancer theranostics Biomaterials 266 120474

- [34] Di X, Pei Z, Pei Y and James T D 2023 Tumor microenvironment-oriented MOFs for chemodynamic therapy Coord. Chem. Rev. 484 215098
- [35] Dong M-J, Li W, Xiang Q, Tan Y, Xing X, Wu C, Dong H and Zhang X 2022 Engineering metal-organic framework hybrid AIEgens with tumor-activated accumulation and emission for the image-guided GSH depletion ROS therapy ACS Appl. Mater. Interfaces 14 29599–612
- [36] Bai J, Peng C, Guo L and Zhou M 2019 Metal-organic framework-integrated enzymes as bioreactor for enhanced therapy against solid tumor via a cascade catalytic reaction ACS Biomater. Sci. Eng. 5 6207–15
- [37] Wang Y, Gao N, Li X, Ling G and Zhang P 2024 Metal organic framework-based variable-size nanoparticles for tumor microenvironment-responsive drug delivery *Drug. Deliv. Trans. Res.* 14 1737–55
- [38] Wang L, Xu Y, Liu C, Si W, Wang W, Zhang Y, Zhong L, Dong X and Zhao Y 2022 Copper-doped MOF-based nanocomposite for GSH depleted chemo/photothermal/chemodynamic combination therapy Chem. Eng. J. 438 135567
- [39] Wu W, Yu L, Jiang Q, Huo M, Lin H, Wang L, Chen Y and Shi J 2019 Enhanced tumor-specific disulfiram chemotherapy by in situ Cu²⁺ chelation-initiated nontoxicity-to-toxicity transition *J. Am. Chem. Soc.* 141 11531–9

- [40] Zhang J, Li P, Wang T, Li J, Yun K, Zhang X and Yang X 2023 A copper nanocluster-based multifunctional nanoplatform for augmented chemo/chemodynamic/photodynamic combination therapy of breast cancer *Pharmacol. Res.* 187 106632
- [41] Li X, Xi D, Yang M, Sun W, Peng X and Fan J 2021 An organic nanotherapeutic agent self-assembled from cyanine and Cu (II) for combined photothermal and chemodynamic therapy Adv. Healthcare Mater. 10 2101008
- [42] Sang D, Wang K, Sun X, Wang Y, Lin H, Jia R and Qu F 2021 NIR-driven intracellular photocatalytic O₂ evolution on Z-scheme Ni₃S₂/Cu_{1.8}S@HA for hypoxic tumor therapy ACS Appl. Mater. Interfaces 13 9604–19
- [43] Chuan D, Hou H, Wang Y, Mu M, Li J, Ren Y, Zhao N, Han B, Chen H and Guo G 2023 Multifunctional metal-polyphenol nanocomposite for melanoma targeted photo/chemodynamic synergistic therapy J. Mater. Sci. Technol. 152 159–68
- [44] Hao Y-N, Qu C-C, Shu Y, Wang J-H and Chen W 2021 Construction of novel nanocomposites (Cu-MOF/GOD@HA) for chemodynamic therapy Nanomaterials 11 1843
- [45] Zhang H, Tang W, Gong Q, Yang X, Sun Y, Dai Z, Hu Z and Zheng X 2022 A dual gate-controlled intelligent nanoreactor enables collaborative precise treatment for cancer nanotherapy *Nanoscale* 14 13113–22